

Cite this: DOI: 00.0000/xxxxxxxxxx

Mesoscale Interplay Between Phonons and Crystal Electric Field Excitations in Quantum Spin Liquid Candidate₂[†]

Yun-Yi Pai,^{a,b} Claire E. Marvinney,^{a,b} Liangbo Liang,^c Jie Xing,^a Allen Scheie,^d Alexander A. Poretzky,^c Gábor B. Halász,^{a,b} Xun Li,^a Rinkle Juneja,^a Athena S. Sefat,^a David Parker,^a Lucas Lindsay,^a and Benjamin J. Lawrie^{a,b}

Received Date

Accepted Date

DOI: 00.0000/xxxxxxxxxx

CsYbSe₂, a recently identified quantum spin liquid (QSL) candidate, exhibits strong crystal electric field (CEF) excitations. Here, we identify phonon and CEF modes with Raman spectroscopy and observe strong CEF-phonon coupling resulting in a vibronic bound state. Complex, mesoscale interplay between phonon modes and CEF modes is observed in real space. Additionally, unexpected resonant Raman excitation condition is satisfied, yielding up to third-order combination modes, with a total of 17 modes identified in the spectra. This study paves the way to coherent control of possible QSL ground states with optically accessible CEF-phonon manifolds and mesoscale engineering of CEF-phonon interactions.

1 Introduction

Quantum spin liquids (QSLs) have been a topic of intense research interest in condensed matter physics in recent decades^{1–3}. The still elusive possibility of control over distributed many-body entanglement offers a key path toward fault-tolerant registers for quantum information processing. Quantum spin liquid candidates like α -RuCl₃^{4–12}, κ -(BEDT-TTF)₂Cu₂(CN)₃¹³, and YbMgGaO₄¹⁴ typically exhibit geometric frustration of some sort, but there have not yet been conclusive observations of QSLs, nor are there well accepted measurement protocols for QSL order parameters.

Yb delafossites¹⁵ such as NaYbS₂^{16,17}, NaYbSe₂^{18–20},

NaYbO₂^{21,22}, CsYbSe₂^{23–26}, and KYbSe₂^{27,28} - with effective spin $S_{\text{eff}} = 1/2$ from Yb³⁺ ions and antiferromagnetic coupling decorating 2D triangular lattices - are popular QSL candidates. Easy-plane magnetic anisotropy results in a plateau at one-third of the saturation magnetization due to strong spin fluctuations^{19,21–23}. There have been no reports of long-range magnetic ordering at temperatures as low as $T = 0.4$ K as a result of the geometric frustration in these materials. This family is thought to be less defect prone than QSL candidate YbMgGaO₄^{23,25,26,29}.

Crystal electric field (CEF) modes emerge as a result of the lifting of the orbital degeneracy of transition metal ions in their ligand environments^{30,31}. CEFs can therefore be used as probes of internal fields. Lower energy CEFs are particularly important as they are part of the ground state wavefunction that defines properties such as magnetism, conductivity and superconductivity³². For instance, the CEF splitting and spin-orbit coupling of Yb³⁺ 4f¹³ orbitals causes the intrinsic magnetic anisotropy in Yb delafossites. CEF modes are also responsible for a Schottky anomaly that has been observed in some members of this family. The rare earth Yb³⁺ doublets are time-reversal degenerate Kramers pairs³³. The 4f electrons - well shielded compared to 3d electrons - exhibit smaller CEF splitting³⁴. CEF excitations can also interact with other excitations in the system^{35–37}. While CEFs have been extensively studied since the 60s, understanding of their interactions with other excitations beyond pristine single ion environments remains rather limited. CEF coupling to electron-hole pairs has been proposed as the mechanism that mediates superconductivity in UPd₂Al₃^{38–41} and PrOs₄Sb₁₂⁴². It was reported for Pr(Os_{1-x}Ru_x)₄Sb₁₂ that, when CEF and phonon modes

^a Materials Science and Technology Division, Oak Ridge National Laboratory, Oak Ridge, TN 37831, USA; E-mail: yunyip@ornl.gov; lawrie@ornl.gov

^b Quantum Science Center, Oak Ridge, Tennessee 37831, USA

^c Center for Nanophase Materials Sciences, Oak Ridge National Laboratory, Oak Ridge, TN 37831, USA

^d Neutron Scattering Division, Oak Ridge National Laboratory, Oak Ridge, TN 37831, USA

[†] Electronic Supplementary Information (ESI) available: (1) data for the figures in the main manuscript can be accessed at <https://github.com/yypai/CsYbSe2>, (2) Raman tensor analysis, polarization dependence, etc. See Supplemental Materials DOI: 00.0000/00000000.

‡ This manuscript has been authored by UT-Battelle, LLC, under contract DE-AC05-00OR22725 with the US Department of Energy (DOE). The US government retains and the publisher, by accepting the article for publication, acknowledges that the US government retains a nonexclusive, paid-up, irrevocable, worldwide license to publish or reproduce the published form of this manuscript, or allow others to do so, for US government purposes. DOE will provide public access to these results of federally sponsored research in accordance with the DOE Public Access Plan (<http://energy.gov/downloads/doe-public-access-plan>).

cross each other, the superconducting transition temperature has a minimum⁴³.

When the mode energy of a CEF and that of a phonon mode are close to each other, mode resonance can happen. This strong CEF-phonon coupling may even yield vibronic bound states. CEF-phonon coupling has been observed in CeAuAl₃^{36,44}, Ce₂O₃³⁵, CeAl₂^{45–47}, PrNi₅⁴⁸, NdBa₂Cu₃O_{7– δ} ⁴⁹, and Ho₂Ti₂O₇⁵⁰, among other materials. Conduction electrons may further complicate the picture and alter the relative intensity of hybrid modes⁵¹. Understanding the complex manifold spanned by CEFs and phonons, their interactions, and their associated optical selection rules may lead to emergent functionalities that take advantage of spin-lattice coupling. Also, this understanding may be useful for controlling and reading out possible QSL ground states for topological quantum information processing.

Inelastic scattering methods such as neutron and Raman scattering are workhorse tools for probing fundamental excitations such as phonons, CEF modes⁵², magnons, and possible Majorana states^{7,53}. Though Raman spectroscopy typically probes excitations near the Γ point in the Brillouin zone, it is capable of probing higher energy modes that are challenging to access with neutron scattering. Further, Raman microscopy can be used to probe sub-micron-scale spatial variation to reveal interactions between excitations. Here, we employ polarization-, spatially-, and temperature-resolved Raman spectroscopy to probe CEF-phonon interactions in CsYbSe₂. We identify all the primary phonons, and CEFs. We report combination modes as a result of resonant Raman condition, a vibronic bound state as a result of mode resonance, and mode repulsion between CEF and phonon modes. Our work extends explorations of CEF-phonon coupling into the emerging class of candidate QSLs.

2 Methods

2.1 Sample Details and Experimental Setup

High quality single crystal CsYbSe₂ (Figure 1) was grown using a previously described flux method²⁶. Polarization-resolved Raman spectra from $T = 3.3$ K - 300 K were taken in a Montana Instruments closed-cycle cryostat with out-of-plane excitation and a back scattering geometry (beam path \parallel c). The spectra were measured with a Princeton Instruments Isoplane SCT-320 spectrograph with a Pixis 400BR Excelon camera and a 2400 line/mm grating. A 532.03 nm continuous wave laser excitation and a set of 3 Optigrate volume Bragg gratings were used to access low energy Stokes and anti-Stokes Raman modes. Achromatic half-wave plates were mounted on piezoelectric rotators for polarization control. The power at the sample was about 1.5 mW and the typical acquisition time was about 30 sec per spectrum. The hyperspectral Raman microscopy was performed with an AttoCube 3-axis positioner and Semrock filters in lieu of the Bragg gratings (for improved collection efficiency).

2.2 Calculation Details

To obtain frequencies and vibration patterns of Raman-active phonon modes in CsYbSe₂, first-principles plane-wave density functional theory (DFT) calculations were performed using VASP

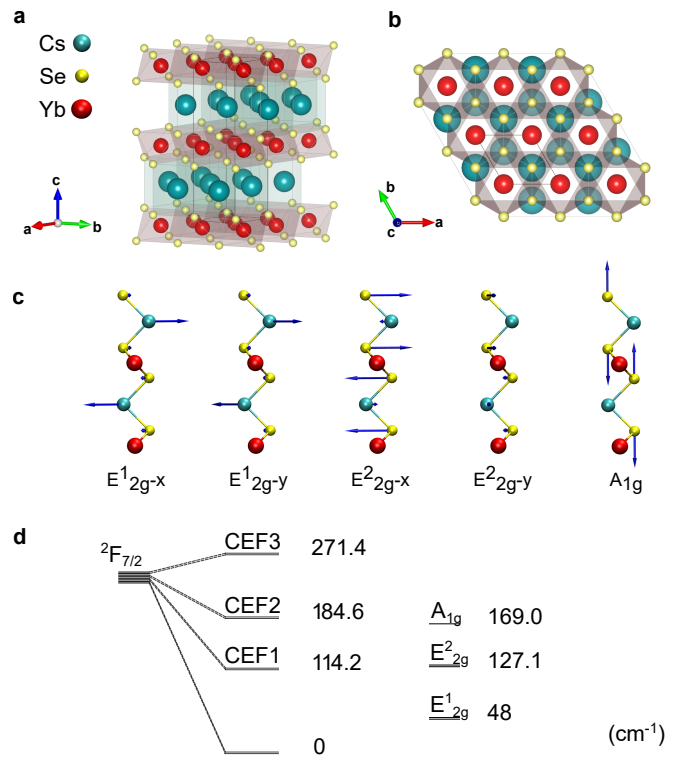


Fig. 1 (a) Side view and (b) top view of the crystal structure of CsYbSe₂. (c) Vibration patterns of Raman active phonon modes in CsYbSe₂. (d) Primary CEF excitations and phonon excitations.

software with projector augmented wave (PAW) pseudopotentials for electron-ion interactions⁵⁴ and the Perdew-Burke-Ernzerhof (PBE) functional for exchange-correlation interactions⁵⁵. The DFT+U method was used to consider the localized f electrons of Yb atoms, with the effective U parameter chosen as 6.0 eV⁵⁶. Other U values including 4.0, 5.0, and 7.0 eV were tested as well, which yielded the same phonon frequencies. It is worth noting that, recent studies on similar materials using a hybrid PBE0 functional⁵⁷ and self-interaction corrected functionals⁵⁸ have shown better agreement with experimental electronic and structural properties compared to the Hubbard correction (DFT+U). Both atomic coordinates and lattice constants were optimized until the residual forces were below 0.001 eV/Å, with a cutoff energy of 400 eV and a Γ -centered k-point sampling of $18 \times 18 \times 5$. The total energy was converged to 10^{-8} eV. Based on the optimized unit cell, we then performed phonon calculations using a finite-difference scheme implemented in Phonopy⁵⁹. The same cutoff energy and convergence criteria of energy were used. Hellmann-Feynman forces in the $3 \times 3 \times 1$ supercell with a Γ -centered k-point sampling of $6 \times 6 \times 5$ were computed by VASP for both positive and negative atomic displacements ($\delta = 0.03$ Å) and then used in Phonopy to construct the dynamical matrix. The diagonalization of the dynamical matrix provides phonon frequencies and eigenvectors (calculation results in Supplemental Information).^{57,58}

3 Results and Discussion

3.1 Theoretical analysis of phonon and CEF modes

Figures 1 (a) and (b) show the crystal structure of CsYbSe₂. According to group theory and our first-principles phonon calculations, CsYbSe₂ belongs to the space group $P6_3/mmc$ (No. 194) with the point group D_{6h} . The bulk unit cell has a hexagonal lattice with 8 atoms in total, giving rise to 24 normal phonon modes at the Γ point: $\Gamma(D_{6h}) = A_{1g} + 3A_{2u} + 2B_{1u} + 2B_{2g} + E_{1g} + 2E_{2g} + 3E_{1u} + 2E_{2u}$, where Raman active phonon modes correspond to non-degenerate A_{1g} symmetry modes, doubly degenerate E_{2g} symmetry modes, and doubly degenerate E_{1g} symmetry modes. The intensity of a Raman mode is $I \propto |\mathbf{e}_s \cdot \tilde{R} \cdot \mathbf{e}_i|^2$, where \tilde{R} is the Raman tensor of a phonon mode, and \mathbf{e}_s and \mathbf{e}_i are the electric polarization vectors of the scattered and incident light, respectively^{60,61}. In the back-scattering geometry with linear laser polarization, \mathbf{e}_s and \mathbf{e}_i are in plane. Based on the Raman tensors shown in the Supplemental Information, it is clear that only A_{1g} and E_{2g} phonon modes can appear in the Raman spectra, whereas E_{1g} modes cannot be observed in our experimental configuration. This is common in hexagonal layered materials⁶¹. Our DFT calculated frequencies for the two E_{2g} modes (E_{2g}^1 and E_{2g}^2) are 37 cm⁻¹ and 97 cm⁻¹, and A_{1g} at 122 cm⁻¹. These results are consistent with our experimental Raman observations that will be discussed below.

3.2 Temperature dependence

Temperature dependent Raman spectra acquired in an XX polarization configuration ($\mathbf{e}_s = (1, 0, 0)$, $\mathbf{e}_i = (1, 0, 0)$) from $T = 3.3$ K to $T = 285$ K (1 K step from 3.3 to 30 K, 5K step from 40 K to 285 K) are shown in Figure 2 (a) and (b). The white arrow in (a) and the black arrow in (b) highlight an artifact from the volume Bragg gratings that is unrelated to CsYbSe₂.

A total of 10 Raman modes on the Stokes side are resolved in Figure 2. We assign the three modes at 114 cm⁻¹, 183 cm⁻¹, and 269 cm⁻¹ to CEF1, CEF2, and CEF3 respectively. Since the CEF excitations in CsYbSe₂ are expected to be dominated by Yb³⁺ 4f¹³ orbitals with the electronic ground state $J = 7/2$ manifold that is split into 4 doubly degenerate Kramers pairs (Figure 1 (d)), these three modes and the ground state comprise the expected 4 pairs. The next excited state manifold $J = 5/2$ is expected to be about 10,000 cm⁻¹ higher^{62,63}. Additionally, CEFs typically exhibit strongly temperature-dependent intensity and linewidth³². CEF1-CEF3 soften (shifts toward lower energy) at low temperatures and becomes significantly more prominent in intensity. In particular, CEF1 is more than 15.3 times stronger in intensity at $T = 3.3$ K than at $T = 285$ K. The energy levels for the three CEF1-CEF3 modes are consistent with previous spectroscopies of CEF modes in NaYbSe₂¹⁸ and KYbSe₂²⁸. The CEF1 and CEF2 modes are also consistent with a recent report on CEF levels probed by resonant torsion magnetometry and low field susceptibility measurements that are particularly sensitive to CEF1 and the details of the CEF Hamiltonian²⁴.

Though it is common to fit experimentally observed CEF energy levels to obtain crystal field parameters, three clearly visible CEF peaks provide too little information to constrain a fit to the six nonzero crystal field parameters for the three-fold Yb³⁺ symmetry in CsYbSe₂. Nevertheless, to get an approximate understanding of the CEF ground state, we modeled the CEF Hamiltonian using a point charge model calculated using PyCrystalField software⁶⁴ and the Se environment of CsYbSe₂. To match energy scales, we fitted the Se effective charges to the three measured low-temperature CEF levels. This yielded an effective Se charge of -1.54e for CsYbSe₂. The observed and calculated CEF level energies are in Table 1. The ground states of these models, assuming a quantization axis in the c direction, are

$$|\psi_{\pm}\rangle = \pm 0.968|\pm 7/2\rangle + 0.218|\pm 1/2\rangle \pm 0.128|\pm 5/2\rangle \quad (1)$$

This point charge fit is a crude approximation, and shows an easy-axis ground state. However, the coefficients for the ground state eigenfunction can easily be adjusted to give an easy-plane ground state. Previous experience with these materials^{18,24} shows that their ground states tend to be more isotropic or easy-planar, suggesting that the above point-charge fit is not very accurate.

Based on our DFT phonon calculations discussed above, we assign the E_{2g}^1 mode to the 46 cm⁻¹ peak. Further, we assign the peak at 120 cm⁻¹ at $T = 293$ K to E_{2g}^2 . At first glance, it may seem that this high-temperature mode transitions continuously to the peak at 114 cm⁻¹ at $T = 3.3$ K, which we assigned to CEF1

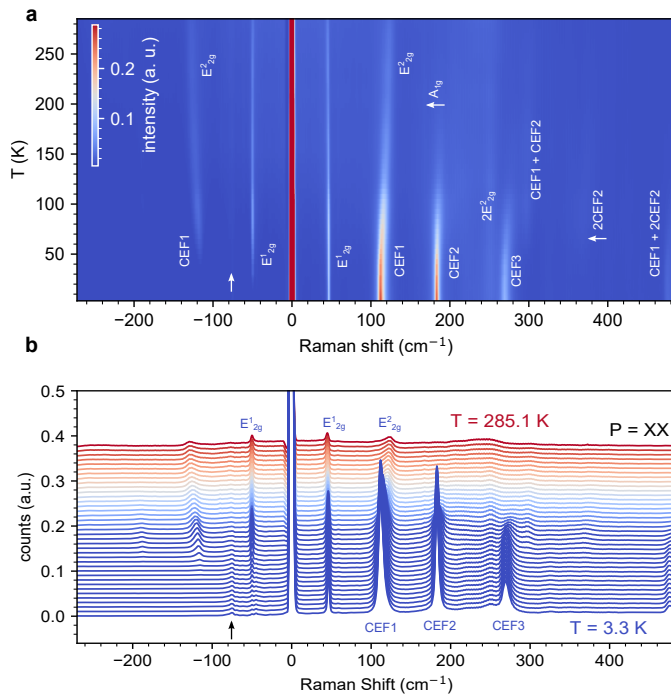


Fig. 2 (a) Temperature dependent Raman spectra from $T = 3.3$ K to $T = 273$ K. The legends correspond to the assignment of the peaks. (b) The line traces of the temperature dependence data from (a) with manual offset added between traces for clarity. The white arrow in (a) and the black arrow in (b) indicate an artifact from volume Bragg gratings that leaked through the spectrometer.

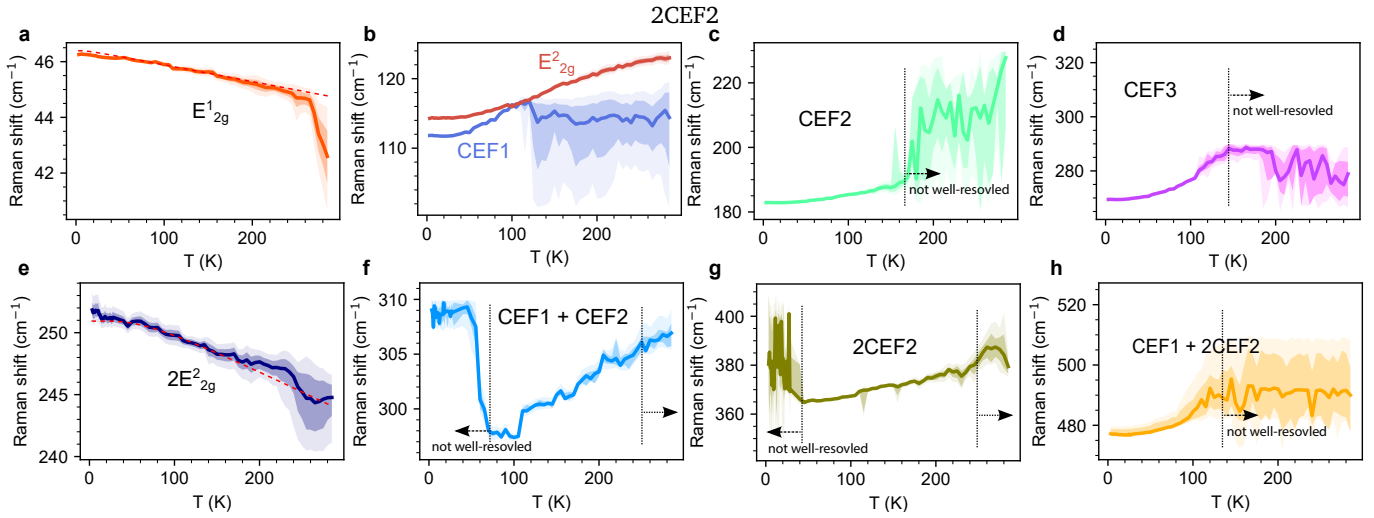


Fig. 3 Peak positions as a function of temperature for the most prominent 9 peaks (extracted from Figure 2, see text) (a) E_{2g}^1 , (b) CEF1 and E_{2g}^2 , (c) CEF2, (d) CEF3, (e) $2E_{2g}^2$, (f) CEF1 + CEF2, (g) $2CEF2$ and (h) CEF1 + $2CEF2$. The peak positions are extracted from Bayesian inference on the data of Figure 2. The shaded intervals are the 68% HDI and 95% HDI. The wide HDIs indicates high uncertainty due to low peak intensity.

because of its strong softening and intensity increase at low temperatures. However, more careful analysis of the Raman spectra (discussed in greater detail below) shows that, at $T = 293$ K, CEF1 is a weak mode nearly resonant with E_{2g}^2 . As the temperature decreases, E_{2g}^2 does not have marked increase in intensity compared to CEF1. The A_{1g} mode is assigned to a small peak at 169.0 cm^{-1} , since this peak shows up in the XX polarization configuration and disappears in the XY polarization configuration, a signature of A_{1g} symmetry according to the group theory analysis discussed below. While this mode is resolved at $T = 293$ K, due to its low intensity and its proximity to CEF2, we were not able to resolve it at low temperatures. We assign the mode 255.9 cm^{-1} to $2E_{2g}^2$, and 300 cm^{-1} to CEF1 + CEF2. The 368.0 cm^{-1} and 479.1 cm^{-1} peaks could be attributed to several higher-order modes including 368.0 cm^{-1} : $2CEF2$, CEF1 + $2E_{2g}^2$, CEF3 + $2E_{2g}^1$ and 479.1 cm^{-1} : CEF1 + $2CEF2$, $2E_{2g}^1$ + $3E_{2g}^2$. We think 368.0 cm^{-1} is likely $2CEF2$, and 479.1 cm^{-1} is likely CEF1 + $2CEF2$ because of their temperature dependence or spatial dependence which we will discuss shortly. We observed and identified 8 more modes in higher energy Raman spectra (Supplemental Information) that we will revisit in Section 3.4.

To further verify the mode assignment and symmetry, we performed polarization-resolved Raman spectroscopy measurements in both parallel (XX) and cross (XY) polarization configurations. According to group theory analysis (more details in Supplemental Information), the polarization profile of an E_{2g} Raman mode is circular under any linear polarization configuration. For an A_{1g} Raman mode, the polarization profile is circular in the XX configuration while its intensity is zero in the XY configuration ($\mathbf{e}_s = (1, 0, 0)$, $\mathbf{e}_i = (0, 1, 0)$). Similar polarization responses of Raman modes have been previously reported for NaYbSe_2 ¹⁸. Under the XX configuration, at room temperature, E_{2g}^1 , E_{2g}^2 , and A_{1g} all have 0-fold symmetry (i.e., circular polarization profiles), and at low temperatures, the E_{2g}^1 , CEF1, CEF2 and CEF3 modes likewise exhibit 0-fold symmetry (Supplemental Information), consistent

with the group theory analysis for these modes. All of the modes above except A_{1g} exhibit nearly the same intensity across the XX and XY configurations while A_{1g} is suppressed in the XY configuration, in agreement with the analysis based on their Raman tensors (Supplemental Information). We note that the polarization profiles of CEF Raman modes are very similar to the polarization profiles of E_{2g} phonon modes, suggesting that CEF modes share similar forms of Raman tensors to E_{2g} phonon modes.

To track the temperature evolution of the observed CEF and phonon modes from the data of Figure 2, we employed Bayesian inference techniques with a Hamiltonian Monte Carlo technique PyMC3⁶⁵, a No U-Turns (NUTS) sampler, and 4 chains with 3,000 samples for spectral modeling. Figure 3 illustrates the inferred peak positions of the most prominent peaks: E_{2g}^1 , E_{2g}^2 , CEF1, CEF2, CEF3, $2E_{2g}^2$, CEF1 + CEF2, $2CEF2$ and CEF1 + $2CEF2$. The traces are the median values from the Bayesian inference. The two shaded bands are 68 % (darker) and 95 % (lighter) highest density intervals (HDIs).

We see:

- Regular phonon modes that are uncoupled to other modes, such as E_{2g}^1 and $2E_{2g}^2$ in Figures 3 (a) and 3(e) respectively, harden (shift toward higher energy) as the temperature decreases. This is the most common temperature dependence for phonons in most materials in general. This temperature dependence usually fits to a phonon anharmonic decay model. The fit to the anharmonic decay model is shown as red dashed line in these two subplots.
- CEF modes shown in Figure 3 (c), (d), (f), (g), (h) soften. The CEF modes are more prominent for $T < 120 - 140$ K and far weaker at higher temperatures. This can be seen in the large uncertainty of the Bayesian inference result for these CEF modes at higher temperatures. The combination modes CEF1 + CEF2 and $2CEF2$ are not well-resolved at lower temperature ($T < 70$ K for CEF1 + CEF2 and $T < 40$ K for

2CEF2). This results in large uncertainties of the Bayesian inference result for these CEF modes as highlighted in Figure 3.

- Coupled phonon-CEF modes such as E_{2g}^2 exhibit a nontrivial temperature dependence that deviates from the phonon anharmonic decay model. For example, phonons coupled to spin degrees of freedom in $\text{RuSr}_2\text{GdCu}_2\text{O}_8$ caused anomalous frequency shifts⁶⁶. Anomalous softening for E_{2g} in NaYbSe_2 due to coupling to CEF1 was also reported recently¹⁸.

3.3 Real space mode repulsion observed with hyperspectral Raman

Mesoscale interplay between CEF and phonon modes is also observed in real-space hyperspectral Raman microscopy of the same flake at $T = 3.3$ K, as shown in Figure 4. The Raman map consists of 45×45 spectra across a $96 \times 88 \mu\text{m}$ area. Selected spectra with distinct representative features are shown in Figure 4 (a).

The spectrum at $(x, y) = (10 \mu\text{m}, 76 \mu\text{m})$ has prominent CEF1, CEF2, and CEF3 modes, consistent with the majority of the 2,025 sampled pixels. While the envelope of all the spectra (illustrated by the shaded background) still exhibits most of the spectral content that is present at each pixel, material heterogeneity induces substantial linewidth broadening in the shaded spectrum. For example, at $(x, y) = (6 \mu\text{m}, 72 \mu\text{m})$, the intensity of the CEF1, CEF2 and CEF3 modes are only about 50 % of their peak intensity, and smaller peaks at 127.1 cm^{-1} and 145.1 cm^{-1} are observed. Additionally, the peaks at 233.9 cm^{-1} and 255.9 cm^{-1} are more prominent. There are also smaller peaks at 383.7 cm^{-1} and 510.7 cm^{-1} . We assign 127.1 cm^{-1} to E_{2g}^2 , which is only a small baseline next to CEF1 at most pixels and 145.1 cm^{-1} to a vibronic bound state ω_2 from the strong coupling between CEF1 and E_{2g}^2 . We further assign 255.9 cm^{-1} , 383.7 cm^{-1} and 510.7 cm^{-1} to $2E_{2g}^2$, $3E_{2g}^2$ and $4E_{2g}^2$, respectively.

To carefully track the spatial dependence of each mode we utilized baseline removal with asymmetric least squares (ALS) and non-negative matrix factorization (NMF). Below we discuss the ALS results. NMF results are described in the Supplementary Information.

Figures 4 (b) - (i) illustrate the Raman intensity maps (red: high; blue: low) for modes (b) CEF1, (c) E_{2g}^2 , (d) ω_2 , (e) CEF2 + E_{2g}^1 , (f) $2E_{2g}^2$, (g) CEF2, (h) CEF3, and (i) CEF1 + 2CEF2. The selected pixels from panel (a) are marked. Spatial anticorrelations between the CEF modes and E_{2g}^2 phonons are observed: where CEF modes are strong, the E_{2g}^2 and $2E_{2g}^2$ modes are weak. This also corroborates our assignment of 479.1 cm^{-1} as CEF1 + 2CEF2 because the mode shows positive spatial correlation with other CEF modes. While there have been many spectroscopic reports of CEF-phonon coupling in other materials, interplay of CEF excitations and phonons in real space has not been previously reported. One possible origin of the inhomogeneity may come from Yb_{Cs} antisite defect, i.e., Yb atoms occupying Cs sites (as Yb_{Na} reported for NaYbSe_2 ²⁰). At $(x, y) = (51 \mu\text{m}, 32 \mu\text{m})$, for example, CEF modes are weakened while phonon modes are strengthened.

This could be explained by a higher density of Yb_{Cs} antisite defects, where Yb ions may have valence Yb^{2+} to neutralize Se^{2-} instead of Yb^{3+} . Since Yb^{2+} has a closed $4f^{14}$ shell, there would be no CEF modes to excite. The CEF mode does not completely disappear because the observed peak height is an ensemble average within the confocal volume. Since the pristine Yb^{3+} - Se^{2-} has a large electron cloud overlap¹⁸, strong electron-phonon coupling is expected, and the Raman intensity of the bare phonon mode may be therefore reduced. With the Yb orbital turned into a closed shell, the electron-phonon coupling that weakened the bare phonon response is removed, resulting in increased intensity. The vibronic bound state is visible when both CEFs and E_{2g}^2 are moderately active, such as at position $(x, y) = (6 \mu\text{m}, 72 \mu\text{m})$. If ω_2 is indeed a vibronic bound state resulting from CEF1 and E_{2g}^2 interactions and tuned by Yb_{Cs} density, it may be possible to engineer the electron-phonon coupling by means of Yb-ion implantation.

3.4 CEF-phonon bound state and combination modes

Vibronic Bound state. When mode resonance between a CEF and a phonon mode happens, vibronic bound states can form. This form of *magnetoelastic* coupling has been detected by Raman spectroscopy since the 80s in CeAl_2 ⁴⁷. There, closely spaced CEF and phonon modes form two new modes with energies described by the Thalmeier-Fulde description⁴⁷:

$$\omega_{1,2} = \frac{\omega_{\text{CEF}} + \omega_{\text{ph}}}{2} \pm \sqrt{\left(\frac{\omega_{\text{CEF}} - \omega_{\text{ph}}}{2}\right)^2 + V^2} \quad (2)$$

where ω_{CEF} and ω_{ph} are the energies of the closely spaced CEF and phonon modes, respectively, and V is the effective coupling strength. With the 145.1 cm^{-1} peak assigned to the ω_2 mode of CEF1 and E_{2g}^2 , we obtain an effective coupling strength of 23.6 cm^{-1} at $T = 3.3$ K, which is smaller than Ce_2O_3 ³⁵ and larger than CeAl_2 ⁴⁷. This model suggests that a conjugate bound state ω_1 exists at 96.2 cm^{-1} , but ω_1 was not observed, potentially due to the 90 cm^{-1} cutoff of the longpass filter that was used for the hyperspectral Raman measurements. It is worth pointing out that ω_2 is observed only in a small subset of the sampled real space positions, such as $(x, y) = (6 \mu\text{m}, 72 \mu\text{m})$, the purple trace in Figure 4 (a) and purple square in the rest of the subplots of Figure 4. The eigenvibration of the E_{2g}^2 mode is described by the out-of-phase vibration of the two Se atoms next to the Yb^{3+} ion, which is responsible for the CEF modes.

Combination modes. Together, a total of 17 modes are observed in Figures 2, 4 and S1. Their energies and assignments are summarized in Table 1. Up to third order combination modes such as CEF1 + 2CEF2, 2CEF2 + CEF3, are identified. Phonon dressed electronic excitations are extremely common in photoluminescence⁶⁷ and ARPES⁶⁸, and combination modes and overtones are also quite common in resonant Raman spectroscopy (the laser must be resonant with a given electronic transition), including CEF modes coupled to LO phonons⁶⁹ and CEF subtraction modes⁷⁰. For the resonant Raman spectroscopy, recently it was reported that for $\text{Ho}_2\text{Ti}_2\text{O}_7$ ⁷¹, 633 nm laser cause excitation resonance because it is close to 5I_8 to 5F_3 transition of $\text{Ho}_2\text{Ti}_2\text{O}_7$.

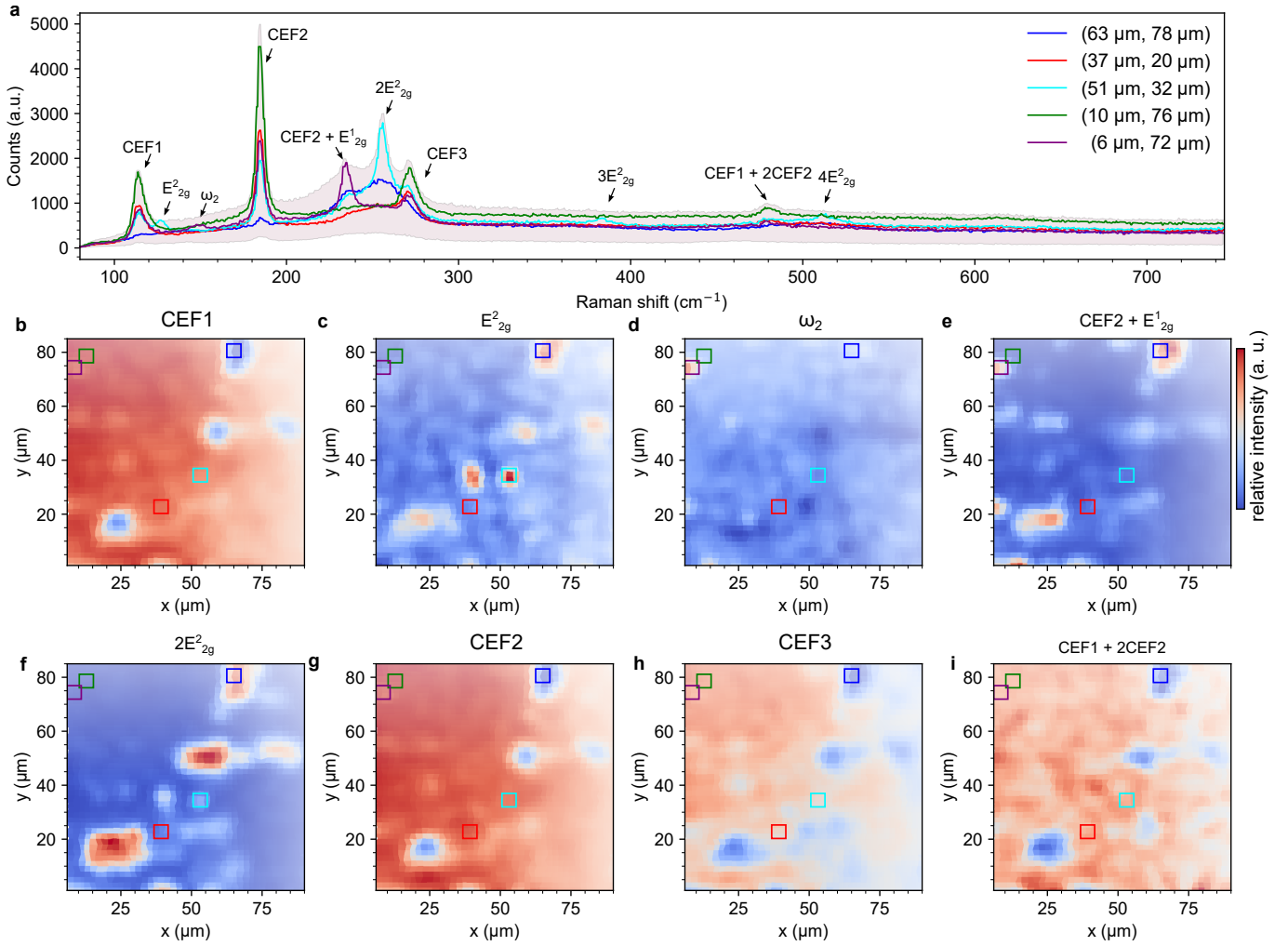


Fig. 4 Hyperspectral Raman map of a $96.1 \mu\text{m}$ by $88.4 \mu\text{m}$ area of the crystal shows subtle mesoscale spatial dependence of the CEF modes and phonon modes. The data was taken with no polarization control. (a) Representative spectra at 5 positions on the sample. (b)-(i) integrated relative intensity of the prominent peaks as a function of position. (b) CEF1, (c) E_{2g}^2 , (d) ω_2 , (e) CEF2 + E_{2g}^1 , (f) $2E_{2g}^2$, (g) CEF2, (h) CEF3, (i) CEF1 + 2CEF2

For CsYbSe_2 , a similar transition from $J = 7/2$ to $J = 5/2$ manifold may happen but it has energy around $\sim 1 \text{ eV}$ so our 532 nm (2.33 eV) excitation will not result in resonant Raman condition.

Alternatively, the electronic gap of NaYbSe_2 is 1.92 eV ²⁹. If CsYbSe_2 has a similar electronic gap, the laser excitation (532 nm , 2.33 eV) should generate photocarriers that can scatter more strongly with phonons and CEF modes compared to non-resonant Raman, leading to an increased probability of higher-order scattering events. The relative intensity of the various combination modes is not well understood, but we hypothesize that it is related to the mode resonance between CEF1 and E_{2g}^2 . Because of the close spectral overlap between those modes and because of the resulting large scattering cross section, we expect the higher order modes are mainly populated by the CEF1 and E_{2g}^2 instead of any other modes.

4 Conclusion

We identified all the primary CEF and phonon modes for QSL candidate CsYbSe_2 and verified their symmetries. Interestingly,

with sub-micron spot size, we observed mesoscale spatial mode repulsion between CEFs and phonon modes. Furthermore, we identified a CEF-phonon bound state ω_2 from CEF1 and E_{2g}^2 and extracted an effective coupling strength $V = 23.58 \text{ cm}^{-1}$. Unexpected resonant Raman condition is satisfied yielding up to third order combination modes. These results for the magnetoelastic coupling in CsYbSe_2 can be used to estimate the coupling between phonons and potential spinons which may enable the confirmation of the underlying QSL ground state^{72,73}. Understanding the mechanism behind the mesoscale CEF-phonon coupling with knowledge of the complex CEF and phonon manifolds may provide a pathway to optically addressable mesoscale quantum spin devices that take advantage of the QSL ground state.

Author Contributions

All authors discussed the results thoroughly. Y.-Y. P., C. E. M., and B. J. L. performed most of the measurements. L. L. performed Raman tensor analysis. J. X. grew the samples. A. S. performed crystal field analysis. Y.-Y. P, L. L. did majority of the data analysis

wavenumber (cm^{-1})	assignment
48.0	E_{2g}^1
96.2	ω_1 from CEF1 and E_{2g}^2 ($V = 23.5839$)
114.2	CEF1
127.1	E_{2g}^2
145.1	ω_2 from CEF1 and E_{2g}^2 ($V = 23.5839$)
169.0	A_{1g} (293 K)
184.6	CEF2
233.9	CEF2 + E_{2g}^1
255.9	$2E_{2g}^2$
271.4	CEF3
300.0	CEF1 + CEF2
368.0	2CEF2, CEF1 + $2E_{2g}^2$, CEF3 + $2E_{2g}^1$
383.7	$3E_{2g}^2$, CEF1 + CEF3
479.1	CEF1 + 2CEF2, $2E_{2g}^1$ + $3E_{2g}^2$
510.7	$4E_{2g}^2$
615.4	CEF2 + E_{2g}^1 + $3E_{2g}^2$, 3CEF1 + CEF3
639.6	2CEF2 + CEF3, $5E_{2g}^2$

Table 1 Summary of assignments of the observed modes. For some peaks, 368.0 cm^{-1} for example, more than one combinations are possible. We suggest that 368.0 cm^{-1} is likely 2CEF2 and 479.1 cm^{-1} is likely CEF1 + 2CEF2 because of their temperature or spatial dependence. We think that the combination modes with CEF1 and E_{2g}^2 are more likely.

with inputs from A. A. P., X. L., R. J., L. L. performed DFT phonon calculations. A. S. S., D. P., L. L. and B. J. L. initiated and oversaw the project. Y.-Y. P., L.L., B. J. L. wrote most of the manuscript with contributions from all authors.

Conflicts of interest

The authors declare no competing interests.

Acknowledgements

This research was sponsored by the U. S. Department of Energy, Office of Science, Basic Energy Sciences, Materials Sciences and Engineering Division. The first-principles phonon calculations and Raman microscopy were performed at the Center for Nanophase Materials Sciences, which is a U.S. Department of Energy Office of Science User Facility. L.L. acknowledges computational resources of the Compute and Data Environment for Science (CADES) at the Oak Ridge National Laboratory, which is supported by the Office of Science of the U.S. Department of Energy under Contract No. DE-AC05-00OR22725. Postdoctoral research support was provided by the Intelligence Community Postdoctoral Research Fellowship Program at the Oak Ridge National Laboratory, administered by Oak Ridge Institute for Science and Education through an interagency agreement between the U.S. Department of Energy and the Office of the Director of National Intelligence.

Notes and references

- 1 P. Anderson, *Materials Research Bulletin*, 1973, **8**, 153–160.
- 2 J. Knolle and R. Moessner, *Annual Review of Condensed Matter Physics*, 2019, **10**, 451–472.

- 3 L. Savary and L. Balents, *Reports on Progress in Physics*, 2016, **80**, 016502.
- 4 Y. Kasahara, T. Ohnishi, Y. Mizukami, O. Tanaka, S. Ma, K. Sugii, N. Kurita, H. Tanaka, J. Nasu and Y. Motome, *Nature*, 2018, **559**, 227–231.
- 5 L. J. Sandilands, Y. Tian, K. W. Plumb, Y.-J. Kim and K. S. Burch, *Physical Review Letters*, 2015, **114**, 147201.
- 6 Y. Wang, G. B. Osterhoudt, Y. Tian, P. Lampen-Kelley, A. Banerjee, T. Goldstein, J. Yan, J. Knolle, H. Ji, R. J. Cava, J. Nasu, Y. Motome, S. E. Nagler, D. Mandrus and K. S. Burch, *npj Quantum Materials*, 2020, **5**, 14.
- 7 D. Wulferding, Y. Choi, S.-H. Do, C. H. Lee, P. Lemmens, C. Faugeras, Y. Gallais and K.-Y. Choi, *Nature Communications*, 2020, **11**, 1603.
- 8 A. Banerjee, C. A. Bridges, J. Q. Yan, A. A. Aczel, L. Li, M. B. Stone, G. E. Granroth, M. D. Lumsden, Y. Yiu, J. Knolle, S. Bhattacharjee, D. L. Kovrizhin, R. Moessner, D. A. Tennant, D. G. Mandrus and S. E. Nagler, *Nature Materials*, 2016, **15**, 733–740.
- 9 A. Banerjee, J. Yan, J. Knolle, C. A. Bridges, M. B. Stone, M. D. Lumsden, D. G. Mandrus, D. A. Tennant, R. Moessner and S. E. Nagler, *Science*, 2017, **356**, 1055–1059.
- 10 S. H. Baek, S. H. Do, K. Y. Choi, Y. S. Kwon, A. U. B. Wolter, S. Nishimoto, J. van den Brink and B. Buchner, *Physical Review Letters*, 2017, **119**, 037201.
- 11 N. Janša, A. Zorko, M. Gomilšek, M. Pregelj, K. W. Krämer, D. Biner, A. Biffin, C. Rüegg and M. Klanjšek, *Nature Physics*, 2018, **14**, 786–790.
- 12 Y.-Y. Pai, C. E. Marvinney, M. A. Feldman, B. Lerner, Y. S. Phang, K. Xiao, J. Yan, L. Liang, J. Lapano, M. Brahlek and B. J. Lawrie, *The Journal of Physical Chemistry C*, 2021, **125**, 25687–25694.
- 13 B. Miksch, A. Pustogow, M. J. Rahim, A. A. Bardin, K. Kanoda, J. A. Schlueter, R. Hübner, M. Scheffler and M. Dressel, *Science*, 2021, **372**, 276–279.
- 14 Y. Shen, Y.-D. Li, H. Wo, Y. Li, S. Shen, B. Pan, Q. Wang, H. C. Walker, P. Steffens, M. Boehm, Y. Hao, D. L. Quintero-Castro, L. W. Harriger, M. D. Frontzek, L. Hao, S. Meng, Q. Zhang, G. Chen and J. Zhao, *Nature*, 2016, **540**, 559–562.
- 15 B. Schmidt, J. Sichelschmidt, K. M. Ranjith, T. Doert and M. Baenitz, *Phys. Rev. B*, 2021, **103**, 214445.
- 16 M. Baenitz, P. Schlender, J. Sichelschmidt, Y. A. Onykiienko, Z. Zangeneh, K. M. Ranjith, R. Sarkar, L. Hozoi, H. C. Walker, J.-C. Orain, H. Yasuoka, J. van den Brink, H. H. Klauss, D. S. Inosov and T. Doert, *Phys. Rev. B*, 2018, **98**, 220409.
- 17 R. Sarkar, P. Schlender, V. Grinenko, E. Haeussler, P. J. Baker, T. Doert and H.-H. Klauss, *Phys. Rev. B*, 2019, **100**, 241116.
- 18 Z. Zhang, X. Ma, J. Li, G. Wang, D. T. Adroja, T. P. Perring, W. Liu, F. Jin, J. Ji, Y. Wang, Y. Kamiya, X. Wang, J. Ma and Q. Zhang, *Phys. Rev. B*, 2021, **103**, 035144.
- 19 K. M. Ranjith, S. Luther, T. Reimann, B. Schmidt, P. Schlender, J. Sichelschmidt, H. Yasuoka, A. M. Strydom, Y. Skourski, J. Wosnitzer, H. Kühne, T. Doert and M. Baenitz, *Phys. Rev. B*, 2019, **100**, 224417.
- 20 P.-L. Dai, G. Zhang, Y. Xie, C. Duan, Y. Gao, Z. Zhu, E. Feng,

- Z. Tao, C.-L. Huang, H. Cao, A. Podlesnyak, G. E. Granroth, M. S. Everett, J. C. Neufeind, D. Voneshen, S. Wang, G. Tan, E. Morosan, X. Wang, H.-Q. Lin, L. Shu, G. Chen, Y. Guo, X. Lu and P. Dai, *Phys. Rev. X*, 2021, **11**, 021044.
- 21 L. Ding, P. Manuel, S. Bachus, F. Grußler, P. Gegenwart, J. Singleton, R. D. Johnson, H. C. Walker, D. T. Adroja, A. D. Hillier and A. A. Tsirlin, *Phys. Rev. B*, 2019, **100**, 144432.
- 22 K. M. Ranjith, D. Dmytriieva, S. Khim, J. Sichelschmidt, S. Luther, D. Ehlers, H. Yasuoka, J. Wosnitza, A. A. Tsirlin, H. Kühne and M. Baenitz, *Phys. Rev. B*, 2019, **99**, 180401.
- 23 J. Xing, L. D. Sanjeeva, J. Kim, G. R. Stewart, A. Podlesnyak and A. S. Sefat, *Phys. Rev. B*, 2019, **100**, 220407.
- 24 C. A. Pocs, P. E. Siegfried, J. Xing, A. S. Sefat, M. Hermele, B. Normand and M. Lee, *Systematic fitting of crystal-field levels and accurate extraction of quantum magnetic models in triangular-lattice delafossites*, 2021.
- 25 T. Xie, J. Xing, S. E. Nikitin, S. Nishimoto, M. Brando, P. Khanenko, J. Sichelschmidt, L. D. Sanjeeva, A. S. Sefat and A. Podlesnyak, *Field-Induced Spin Excitations in the Spin-1/2 Triangular-Lattice Antiferromagnet CsYbSe₂*, 2021.
- 26 J. Xing, L. D. Sanjeeva, J. Kim, G. R. Stewart, M.-H. Du, F. A. Reboredo, R. Custelcean and A. S. Sefat, *ACS Materials Letters*, 2020, **2**, 71–75.
- 27 J. Xing, L. D. Sanjeeva, A. F. May and A. S. Sefat, *Synthesis and Anisotropic Magnetism in Quantum Spin Liquid Candidates AYbSe₂ (A = K and Rb)*, 2021.
- 28 A. O. Scheie, E. A. Ghioldi, J. Xing, J. A. M. Paddison, N. E. Sherman, M. Dupont, D. Abernathy, D. M. Pajerowski, S.-S. Zhang, L. O. Manuel, A. E. Trumper, C. D. Pemmaraju, A. S. Sefat, D. S. Parker, T. P. Devereaux, J. E. Moore, C. D. Batista and D. A. Tennant, *Witnessing quantum criticality and entanglement in the triangular antiferromagnet KYbSe₂*, 2021.
- 29 W. Liu, Z. Zhang, J. Ji, Y. Liu, J. Li, X. Wang, H. Lei, G. Chen and Q. Zhang, 2018, **35**, 117501.
- 30 H. Bethe, *Annalen der Physik*, 1929, **395**, 133–208.
- 31 J. H. Van Vleck, *Phys. Rev.*, 1932, **41**, 208–215.
- 32 G. Schaack, in *Raman scattering by crystal-field excitations*, Springer, 2000, pp. 24–173.
- 33 H. A. Kramers, *Proc. Acad. Amst.*, 1930, **33**, year.
- 34 D. Parker, E. A. Suturina, I. Kuprov and N. F. Chilton, *Accounts of Chemical Research*, 2020, **53**, 1520–1534.
- 35 A. Sethi, J. E. Slimak, T. Kolodiazhnyi and S. L. Cooper, *Phys. Rev. Lett.*, 2019, **122**, 177601.
- 36 P. Čermák, A. Schneidewind, B. Liu, M. M. Koza, C. Franz, R. Schönmann, O. Sobolev and C. Pfleiderer, *Proceedings of the National Academy of Sciences*, 2019, **116**, 6695–6700.
- 37 D. Adroja, A. del Moral, C. de la Fuente, A. Fraile, E. Goremychkin, J. Taylor, A. Hillier and F. Fernandez-Alonso, *Physical review letters*, 2012, **108**, 216402.
- 38 E. Blackburn, A. Hiess, N. Bernhoeft and G. H. Lander, *Phys. Rev. B*, 2006, **74**, 024406.
- 39 K. Iwasa, K. Saito, Y. Murakami and H. Sugawara, *Phys. Rev. B*, 2009, **79**, 235113.
- 40 N. K. Sato, N. Aso, K. Miyake, R. Shiina, P. Thalmeier, G. Varelogiannis, C. Geibel, F. Steglich, P. Fulde and T. Komatsubara, *Nature*, 2001, **410**, 340–343.
- 41 P. Thalmeier, *The European Physical Journal B - Condensed Matter and Complex Systems*, 2002, **27**, 29–48.
- 42 E. D. Bauer, N. A. Frederick, P.-C. Ho, V. S. Zapf and M. B. Maple, *Phys. Rev. B*, 2002, **65**, 100506.
- 43 R. Miyazaki, Y. Aoki, D. Kikuchi, H. Sugawara and H. Sato, 2010, **200**, 012125.
- 44 B.-Q. Liu, P. Čermák, C. Franz, C. Pfleiderer and A. Schneidewind, *Phys. Rev. B*, 2018, **98**, 174306.
- 45 M. Loewenhaupt, B. D. Rainford and F. Steglich, *Phys. Rev. Lett.*, 1979, **42**, 1709–1712.
- 46 G. Güntherodt, A. Jayaraman, G. Batlogg, M. Croft and E. Melcher, *Phys. Rev. Lett.*, 1983, **51**, 2330–2332.
- 47 P. Thalmeier and P. Fulde, *Phys. Rev. Lett.*, 1982, **49**, 1588–1591.
- 48 V. Aksenov, E. Goremychkin, E. Mühle, T. Frauenheim and W. Bührer, *Physica B+C*, 1983, **120**, 310–313.
- 49 E. T. Heyen, R. Wegerer and M. Cardona, *Phys. Rev. Lett.*, 1991, **67**, 144–147.
- 50 J. Gaudet, A. M. Hallas, C. R. C. Buhariwalla, G. Sala, M. B. Stone, M. Tachibana, K. Baroudi, R. J. Cava and B. D. Gaulin, *Phys. Rev. B*, 2018, **98**, 014419.
- 51 G. Güntherodt, A. Jayaraman, E. Anastassakis, E. Bucher and H. Bach, *Phys. Rev. Lett.*, 1981, **46**, 855–858.
- 52 M. V. Klein, in *Electronic Raman scattering*, ed. M. Cardona, Springer Berlin Heidelberg, Berlin, Heidelberg, 1983, pp. 147–204.
- 53 A. Sahasrabudhe, D. A. S. Kaib, S. Reschke, R. German, T. C. Koethe, J. Buhot, D. Kamenskyi, C. Hickey, P. Becker, V. Tsurkan, A. Loidl, S. H. Do, K. Y. Choi, M. Grüninger, S. M. Winter, Z. Wang, R. Valentí and P. H. M. van Loosdrecht, *Phys. Rev. B*, 2020, **101**, 140410.
- 54 G. Kresse and J. Furthmüller, *Computational Materials Science*, 1996, **6**, 15–50.
- 55 J. P. Perdew, K. Burke and M. Ernzerhof, *Phys. Rev. Lett.*, 1996, **77**, 3865–3868.
- 56 S. L. Dudarev, G. A. Botton, S. Y. Savrasov, C. J. Humphreys and A. P. Sutton, *Phys. Rev. B*, 1998, **57**, 1505–1509.
- 57 E. van Loef, U. Shirwadkar, L. S. Pandian, G. Ciampi, L. Stand, M.-H. Du, M. Koschan, M. Loyd, M. Zhuravleva, C. Melcher and K. Shah, *Nuclear Instruments and Methods in Physics Research Section A: Accelerators, Spectrometers, Detectors and Associated Equipment*, 2021, **995**, 165047.
- 58 R. Shinde, S. S. R. K. C. Yamijala and B. M. Wong, *Journal of Physics: Condensed Matter*, 2020, **33**, 115501.
- 59 A. Togo, F. Oba and I. Tanaka, *Phys. Rev. B*, 2008, **78**, 134106.
- 60 Y. Zhao, X. Luo, H. Li, J. Zhang, P. T. Araujo, C. K. Gan, J. Wu, H. Zhang, S. Y. Quek, M. S. Dresselhaus and Q. Xiong, *Nano Letters*, 2013, **13**, 1007–1015.
- 61 X. Kong, T. Berlijn and L. Liang, *Advanced Electronic Materials*, 2021, **7**, 2001159.
- 62 J. A. Koningstein, *The Journal of Chemical Physics*, 1967, **46**, 2811–2816.

- 63 V. Petit, P. Camy, J.-L. Doualan, X. Portier and R. Moncorgé, *Phys. Rev. B*, 2008, **78**, 085131.
- 64 A. Scheie, *Journal of Applied Crystallography*, 2021, **54**, 356–362.
- 65 J. Salvatier, T. V. Wiecki and C. Fannesbeck, *PeerJ Computer Science*, 2016, **2**, e55.
- 66 A. Fainstein, P. Etchegoin, H. J. Trodahl and J. L. Tallon, *Phys. Rev. B*, 2000, **61**, 15468–15473.
- 67 W. Jin, H. H. Kim, Z. Ye, G. Ye, L. Rojas, X. Luo, B. Yang, F. Yin, J. S. A. Horng, S. Tian, Y. Fu, G. Xu, H. Deng, H. Lei, A. W. Tsen, K. Sun, R. He and L. Zhao, *Nature Communications*, 2020, **11**, 4780.
- 68 C. Chen, J. Avila, S. Wang, Y. Wang, M. Mucha-Kruczyński, C. Shen, R. Yang, B. Nosarzewski, T. P. Devereaux, G. Zhang and M. C. Asensio, *Nano Letters*, 2018, **18**, 1082–1087.
- 69 T. Livneh, *Journal of Physics: Condensed Matter*, 2008, **20**, 085202.
- 70 N. Ogita, R. Kojima, T. Hasegawa, M. Udagawa, H. Sugawara and H. Sato, 2009, **150**, 042147.
- 71 N. Anand, M. Ozerov, L. J. van de Burgt, Z. Lu, J. Holleman, H. Zhou, S. McGill and C. Beekman, *Magnetic field tuning of crystal field levels and vibronic states in Spin-ice Ho₂Ti₂O₇ observed in far-infrared reflectometry*, 2021.
- 72 M. Ye, R. M. Fernandes and N. B. Perkins, *Phys. Rev. Research*, 2020, **2**, 033180.
- 73 K. Feng, M. Ye and N. B. Perkins, *Phys. Rev. B*, 2021, **103**, 214416.